Transient Modeling of Grain Structure and Macrosegregation during Direct Chill Casting of Al-Cu Alloy

Qipeng Chen [1], Hongxiang Li [2] and Houfa Shen [1],*

[1] Key Laboratory for Advanced Materials Processing Technology, Ministry of Education, School of Materials Science and Engineering, Tsinghua University, Beijing 100084, China; chenqp14@mails.tsinghua.edu.cn
[2] State Key Laboratory for Advanced Metals and Materials, University of Science and Technology Beijing, Beijing 100083, China; hxli@skl.ustb.edu.cn
*   Correspondence: shen@tsinghua.edu.cn

Abstract: Grain structure and macrosegregation are two important aspects to assess the quality of direct chill (DC) cast billets, and the phenomena responsible for their formation are strongly interacted. Transient modeling of grain structure and macrosegregation during DC casting is achieved with a cellular automaton (CA)–finite element (FE) model, by which the macroscopic transport is coupled with microscopic relations for grain growth. In the CAFE model, a two-dimensional (2D) axisymmetric description is used for cylindrical geometry, and a Lagrangian representation is employed for both FE and CA calculations. This model is applied to the DC casting of two industrial scale Al-6.0 wt % Cu round billets with and without grain refiner. The grain structure and macrosegregation under thermal and solutal convection are studied. It is shown that the grain structure is fully equiaxed in the grain-refined billet, while a fine columnar grain region and a coarse columnar grain region are formed in the non-grain-refined billet. With the increasing casting speed, grains become finer and grow in a direction more perpendicular to the axis, and the positive segregation near the centerline becomes more pronounced. The increasing casting temperature makes grains coarser and the negative segregation near the surface more pronounced.

Keywords: direct chill casting; solidification; grain structure; macrosegregation; cellular automaton; finite element

1. Introduction

Direct chill (DC) casting is currently the principal processing technology used in the production of wrought aluminum alloys [1], such as cylindrical billets for extrusion and rectangular slabs for rolling. Structure with uniform and equiaxed grains significantly reduces the anisotropy of mechanical properties, improving the plastic processing property. Macrosegregation, i.e., heterogeneities of alloying elements at the casting scale, is bound to occur in large size ingots. As it cannot be mitigated by subsequent treatments, it will lead to nonuniform mechanical properties in final products. Therefore, grain structure and macrosegregation are two important aspects to assess the ingot quality, and uniform fine grains with low segregation of alloying elements are desirable in industrial applications.

The main factors affecting grain structure and macrosegregation include alloying elements and their compositions, billet diameter, casting speed, casting temperature, mold cooling type, and grain refining. Experimental studies [2–9] have provided some insights into the formation mechanisms of grain structure and macrosegregation in DC cast billets. Lesoult et al. [2] investigated the effect of inoculation on the grain structure and centerline segregation in DC cast sheet ingots of an Al-Mg alloy. It was shown that the centerline segregation is more intense in the grain refined ingot. Glenn et al. [3]

found that grain refining has little effect on the dendrite arm spacing but great influence on the grain size and macrosegregation in DC cast ingots of aluminum alloy 5182. Suyitno et al. [4] reported the effects of alloy composition and casting speed on structure formation in DC cast 200-mm round billets of binary Al-Cu alloys. The results showed that the grain structure is strongly affected by the alloy composition and casting speed. Eskin et al. [5] examined the structure formation and marosegregation in Al-4.5 wt % Cu alloy billets cast under different casting speeds and cooling rates. With decreasing casting speed and water-flow rate, coarser grain size and dendritic arm spacing, and less macrosegregation were obtained. The authors also investigated the effects of the melt temperature and casting speed on the structure formation of Al-2.8 wt % Cu alloy billets cast at steady and unsteady stages [6]. They found that the increasing melt temperature deteriorates the subsurface segregation, while it has little effect on the macrosegregation in the rest of the billet. Nadella et al. [7] studied the effects of grain refining and casting speed on structure, "floating" grains, and centerline macrosegregation in DC cast Al-Cu-Mg alloy billets with 192 mm diameter. It was demonstrated that macrosegregation is determined mostly by the casting speed, while the influence of grain refining is negligible. Eskin et al. [8] examined the compositions of coarse-cell and fine-cell dendritic grains in the center of DC cast 2024 aluminum alloy with 200 mm diameter, and found that coarse-cell grains are depleted of solute and contribute to the negative segregation in the central portion of the DC cast ingots.

Modeling and simulation has been a useful tool to gain insight into the intricate phenomena and deepen the understanding of the physical mechanisms in DC casting. A single domain model was first applied to predict macrosegregation in DC cast Al-4.5 wt % Cu billets by Flood et al. [10]. Assuming that the mushy zone consists of a rigid, permeable solid matrix moving at the casting speed, positive segregation of copper was predicted at the center of the billet. Considering the transport of free-floating grains, separate and distinct mixture momentum equations were employed for a slurry and a rigid solid matrix by Vreeman et al. [11,12], and the negative segregation was predicted at the centerline in DC cast Al-4.5 wt % Cu and Al-6.0 wt % Mg billets. Using one-phase continuum mixture model, Zaloznik et al. [13] investigated the effects of the billet diameter, casting temperature, casting speed and mold cooling type on the final macrosegregation in DC cast Al-5.25 wt % Cu alloy billets. The model accounts for the thermosolutal convection and solidification shrinkage. Eskin et al. [14] implemented a multicomponent continuum model and examined the contribution of each solute element to the final segregation pattern in a DC cast Al-Cu-Mg alloy billet. In order to consider the coupling of macrosegregation with grain nucleation, growth, and motion, numerical models that incorporate the macroscopic transports with microscopic relations for grain growth and solutal undercooling have also been developed [15–17]. However, these numerical models are focused on macrosegregation, and the grain structure in the presence of fluid flow and macrosegregation has not been predicted directly. Moreover, most modeling efforts are based on a steady state assumption, and the transient effects are rarely considered [18,19].

Since the phenomena responsible for the formation of grain structure and macrosegregation are closely intertwined during solidification of alloys, a two-dimensional (2D) cellular automaton (CA)–finite element (FE) model [20] has been developed by the authors recently to achieve a direct macroscopic modeling of grain structure and macrosegregation. This contribution is dedicated to extending the CAFE model for a fully transient study of grain structure and macrosegregation during DC casting with a 2D axisymmetric description. A Lagrangian representation is used for both FE and CA calculations, thus the billet can be treated to extend upward from the top surface. The extended CAFE model is applied to the DC casting of two industrial scale Al-6.0 wt % Cu round billets with and without grain refiner [21]. A numerical validation is first performed by comparisons to experimental measured vertical temperature and sump profiles. Then, a transient analysis is presented for the grain-refined billet with regard to the temperature field, grain structure, fluid flow and macrosegregation. Finally, effects of the casting speed and casting temperature on the grain structure and macrosegregation of the non-grain-refined billet are investigated.

2. Model Description

2.1. Macroscopic Transport

The macroscopic transport phenomena are governed by coupled conservation equations of mass, momentum, energy, and solute valid in a mixture of liquid and solid phases. In present work, the continuum mixture model originally formulated by Bennon and Incropera [22] is adopted. The solid phase is assumed as rigid and nondeformable, thus, the mixture in the phase change zone can be regarded as a porous medium, where an isotropic permeability K defined by Carman-Kozeny relation. As a consequence, the macroscopic transport equations formulated in terms of the mixture quantities can be expressed as follows.

Mass conservation:

$$\frac{\partial \rho_m}{\partial t} + \nabla \cdot \left(\rho_m \vec{v}_m\right) = 0, \tag{1}$$

Momentum conservation:

$$\frac{\partial\left(\rho_m \vec{v}_m\right)}{\partial t} + \nabla \cdot \left(\rho_m \vec{v}_m \vec{v}_m\right) = -\nabla p_l + \nabla \cdot \left(\mu_l \frac{\rho_m}{\rho_l} \nabla \vec{v}_m\right) - \frac{\mu_l}{K} \frac{\rho_m}{\rho_l} \vec{v}_m - \rho_l \vec{g}\left[\beta_T(T - T_{\text{ref}}) + \beta_C(C_l - C_{\text{ref}})\right], \tag{2}$$

with:

$$K = \frac{\lambda_2^2 g_l^3}{180(1 - g_l)^2}, \tag{3}$$

Energy conservation:

$$\frac{\partial(\rho_m H_m)}{\partial t} + \nabla \cdot \left(\rho_m \vec{v}_m H_m\right) = \nabla \cdot (\lambda_m \nabla T) - \nabla \cdot \left[\rho_m \vec{v}_m (H_l - H_m)\right], \tag{4}$$

Solute conservation:

$$\frac{\partial(\rho_m C_m)}{\partial t} + \nabla \cdot \left(\rho_m \vec{v}_m C_m\right) = \nabla \cdot (\rho_m f_l D_l \nabla C_m) + \nabla \cdot (\rho_m f_l D_l \nabla(C_l - C_m)) - \nabla \cdot \left(\rho_m \vec{v}_m (C_l - C_m)\right), \tag{5}$$

Auxiliary relations:

$$\begin{array}{llll} \rho_m = g_s \rho_s + g_l \rho_l & \vec{v}_m = f_l \vec{v}_l & H_s = c_{ps} T \\ g_s + g_l = 1 & H_m = f_s H_s + f_l H_l & H_l = c_{ps} T_s + c_{pl}(T - T_s) + \Delta_s^l H_f \\ f_l = \frac{g_l \rho_l}{\rho_m} & C_m = f_s C_s + f_l C_l & C_s = k_p C_l \\ f_s = \frac{g_s \rho_s}{\rho_m} & c_{pm} = f_s c_{ps} + f_l c_{pl} & T_l(C_l) = T_f + m_L C_l \\ & \lambda_m = g_s \lambda_s + g_l \lambda_l & T_s(C_l) = T_f + m_L \frac{C_l}{k_p} \end{array}, \tag{6}$$

In the above formulas, $\vec{v}$ is the velocity, H the enthalpy, C the composition, g the volume fraction, f the mass fraction, ρ the density, λ the thermal conductivity, and c_p the specific heat, with subscripts "m", "l" and "s" denoting values for the mixture, the liquid and the solid respectively. Besides, t is the time, p_l the liquid pressure, μ_l the liquid viscosity, $\vec{g}$ the gravity acceleration, β_T and β_C the thermal and solutal expansion coefficients, T_{ref} and C_{ref} the reference temperature and composition, T the temperature, λ_2 the secondary dendrite arm spacing, T_f the melting temperature of the pure solvent, m_L the liquidus slope in the binary phase diagram, k_p the partition coefficient, and $\Delta_s^l H_f$ is the latent heat of fusion.

2.2. Modeling of Grain Structure

Only metallic materials with cubic crystal system is considered, and the nucleation and growth of one primary dendritic solid phase is modeled. Nucleation sites are spatially distributed in the bulk melt and at the surfaces in contact with the mold. Their density and critical nucleation undercooling follow Gaussian distributions of the melt undercooling [23], which are defined by (ΔT_N^V, ΔT_σ^V, $n_{\max}^V$)

for the bulk melt and (ΔT_N^S, ΔT_σ^S, n_{max}^S) for the surfaces. Here ΔT_N, ΔT_σ and n_{max} are the mean undercooling, the standard deviation and the total density of nucleation sites, with the superscripts "V" and "S" denoting the nucleation laws in the bulk melt and at the surfaces, respectively. Taking the distribution of nucleation sites in the bulk melt for an example, the total number of nuclei is first calculated by the product of the melt volume and the total density n_{max}^V, then all the nuclei are randomly distributed in the bulk melt. For each nucleus, a critical nucleation undercooling is attributed according to the Gauss distribution defined by (ΔT_N^V, ΔT_σ^V, n_{max}^V), and a random crystallographic orientation is given to characterize the dendrite growth direction following a uniform distribution in [0, 90) degrees. Since the 2D case is considered, standard stereological relationships [24] are used to convert the maximum volume density n_{max}^V (m^{-3}) and the maximum surface density n_{max}^S (m^{-2}) into the maximum surface density n_{max}^{V*} (m^{-2}) and the maximum line density n_{max}^{S*} (m^{-1}), respectively. Upon cooling, if a nucleation site is still in liquid state, and if its local undercooling is greater than the critical nucleation undercooling, a new grain is initiated and begins to grow.

A decentered quadrilateral growth algorithm [25] is employed to describe the evolution of a grain envelope outlining the four dendrite tip positions corresponding to the four <01> preferential orientations. The dendrite tip growth velocity is calculated by an extended Lipton–Glicksman–Kurz (LGK) model [20], in which a boundary layer correlation [26] is used for the dimensionless soutal supersaturation Ω_c to consider the intensity and direction of fluid flow as follows:

$$\Omega_c = P_c \exp(P_c)\left\{E_1(P_c) - E_1\left[P_c\left(1 + \frac{4}{A\mathrm{Re}^B\mathrm{Sc}^C \sin\left(\frac{\phi}{2}\right)}\right)\right]\right\}, \tag{7}$$

with:

$$\begin{aligned}
P_c &= \frac{r_p v_p}{2D_l} \\
\mathrm{Re} &= \frac{2r_p v_l}{\frac{\mu_l}{\rho_l}} \\
\mathrm{Sc} &= \frac{\frac{\mu_l}{\rho_l}}{D_l},
\end{aligned} \tag{8}$$

where P_c is the solutal Peclet number, Re the dimensionless Reynolds number, Sc the Schmidt number, r_p the dendrite tip radius, v_p the dendrite tip growth velocity, $\|v_l\|$ the magnitude of the liquid velocity, ϕ the angle between the preferential growth orientation and the flow direction. $E_1(P_c) = \int_{P_c}^{\infty} \frac{\exp(-\tau)}{\tau}d\tau$ is the exponential integral function. Additionally, parameters A, B, and C are taken as 0.5773, 0.6596, and 0.5249, respectively [26]. They were deduced by fitting the Equations (7) and (8) to the exact solutions. Thus, the dendrite tip growth velocity can be expressed as a function of local temperature, average composition, and liquid velocity vector in the presence of fluid flow.

2.3. Solution Algorithm

The coupling of grain structure and macrosegregation is implemented with a CAFE model, which is an extension of a previous study by the authors [20]. The macroscopic transport is solved by a FE method, while the grain structure is described based on a CA method. In order to achieve a fully transient modeling of grain structure and macrosegregation during DC casting, a Lagrangian representation is used for both FE and CA calculations. Figure 1a schematizes a hot-top DC casting considered in present model. It consists of a water-cooled mold, starter block, and water jets. The hot top is a refractory reservoir maintained with a porous graphite "casting ring" inserted in the mold. With a 2D axisymmetric description for cylindrical geometry, the reference frame is attached to the bottom of the billet, as shown in Figure 1b. Thus, the billet can be considered as stationary ($\vec{v}_s = 0$) and growing upward, while the mold moves upward at the casting speed v_{cast}. At each time step,

the molten metal is assumed to be fed uniformly across the entire top surface (inlet) of the growing billet, whose initial height $L_{billet,0}$ is equal to the mold height L_{mold}. The instantaneous height of the growing billet is calculated by:

$$L_{billet} = L_{billet} + v_{cast} \times \Delta t, \tag{9}$$

where Δt is the time step used in the FE calculations. In the FE calculations, a structured FE mesh composed of uniform right triangular elements with a side length l_{FE} is used. In the CA calculations, a CA lattice composed of uniform square cells with a cell size l_{CA} is used, and the CA cell size l_{CA} is smaller than the FE element size l_{FE}. With the billet growing, the FE mesh and the CA lattice extend upward from the top of the billet to cover the entire billet with the height L_{billet}, and the boundary conditions at the top and the lateral surface of the growing billet also move upward.
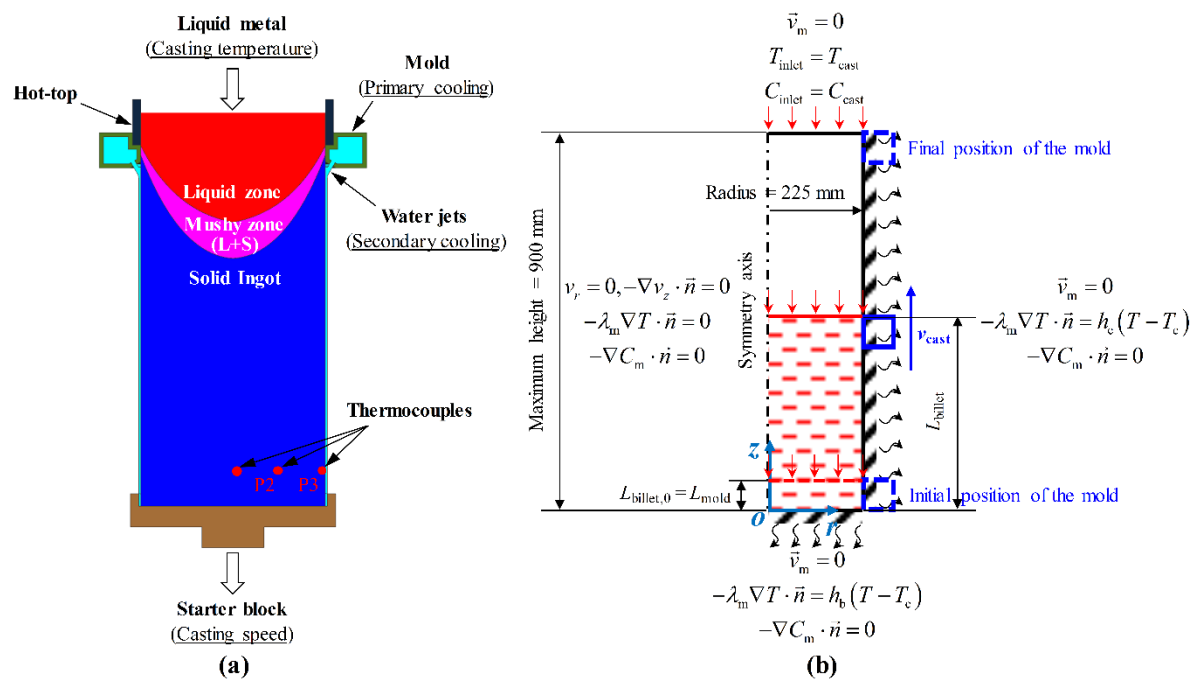

Figure 1. Physical model used in present simulations: (**a**) schematic of a hot-top DC casting process, and (**b**) 2D axisymmetric model with a Lagrangian representation.

Equations (1), (2), (4), and (5) are solved based on the FE mesh. The unknowns in those equations are the average velocity v_m, the intrinsic liquid pressure p_l, the average enthalpy H_m, and the average composition C_m. A fractional step method is applied to Equations (1) and (2) to decouple the velocity and pressure, by which linear equal-order elements are allowed to interpolate the velocity and pressure. Details of the finite element formulations and numerical algorithms are available in reference [27]. The grain structure are tracked based on the CA lattice. Once the average enthalpy H_m, average composition C_m and liquid velocity $\vec{v}_l$ on the FE mesh are obtained by the FE calculations, the corresponding counterparts on the CA lattice are firstly calculated by interpolation from the FE mesh to the CA lattice. Then the nucleation, grain growth and capture, dendrite tip growth velocity, and conversion of enthalpy and composition to temperature and solid fraction are performed on the CA lattice. Finally, the mass fraction of liquid f_l, temperature T, and liquid composition C_l on the FE mesh are calculated by feedback from the CA lattice to the FE mesh. Details of the CA method and its coupling with the FE method can be found in [20].

3. Numerical Setup

Vreeman et al. [21] cast two Al-6.0 wt % Cu round billets of 450 mm diameter using a hot-top DC casting process, as shown in Figure 1a. The mold height L_{mold} is 70 mm, with the top 10 mm

thermally insulated. Identical conditions were used except that only one billet was cast with Al-3 wt % Ti-1 wt % B grain refiner and the other without. Three vertical temperature profiles at different radial positions of 10 mm, 106 mm and 220 mm were recorded by the three thermocouples denoted as P1, P2, and P3, respectively. Moreover, the sump profiles that consist of the liquid zone and the mushy zone were also measured in the two billets. With regard to the grain structure, it was mentioned that the representative grain size for both billets is 75 μm. The grain structure was asserted to be fully equiaxed in the grain-refined billet. For the non-grain-refined billet, however, the grain structure was not clear, and a possible columnar-to-equiaxed transition (CET) was suspected.

The calculation domain with corresponding boundary conditions is shown in Figure 1b. It is assumed that the liquid and solid densities are constant and equal. Thus, a no-slip boundary condition is given at the top of the domain, which is 225 mm in width. As the casting process can be considered steady generally after a length of one billet diameter is cast [1], a maximum height of 900 mm is used in present simulations. The heat extraction by the mold is considered by a zero heat transfer coefficient in the upper 10 mm and a constant heat transfer coefficient of $h_{mold} = 30$ W·m^{-2}·K^{-1} in the lower 60 mm, with the cooling water temperature $T_c = 300$ K. Another constant heat transfer coefficient of $h_b = 400$ W·m^{-2}·K^{-1} is used for the heat extraction by the starter block, with a reference temperature equal to the cooling water temperature T_c. For the heat extraction by the secondary cooling, a heat transfer coefficient distribution similar to the one proposed by Vreeman et al. [12] is taken as follows:

$$
\begin{array}{ll}
h_c = h_{mold} + \frac{L-L_{mold}}{L_{asc}}(h_{max} - h_{mold}), & (L_{mold} \leq L < L_{mold} + L_{asc}) \\
h_c = h_{max} + \frac{L-L_{mold}-L_{asc}}{L_{desc}}(h_{film} - h_{max}), & (L_{mold} + L_{asc} \leq L < L_{mold} + L_{asc} + L_{desc}) \\
h_c = h_{film}, & (L \geq L_{mold} + L_{asc} + L_{desc})
\end{array}
\tag{10}
$$

with:

$$
L = L_{billet} - z,
\tag{11}
$$

where L_{asc} and L_{desc} are characteristic parameters, and h_{max} and h_{film} are the maximum value and uniform value of the heat transfer coefficient, respectively. L_{asc} represents the length for the heat transfer coefficient ascending from h_{mold} to h_{max}, while L_{desc} is the length for the heat transfer coefficient descending from h_{max} to h_{film}. As proposed in [12], L_{asc} and L_{desc} are taken as 10 mm and 40 mm, respectively. However, h_{max} and h_{film} are taken as 25,000 W·m^{-2}·K^{-1} and 15,000 W·m^{-2}·K^{-1}, respectively.

Six cases are considered for Al-6.0 wt % Cu alloy. The simulation parameters identical for all cases are summarized in Table 1, and the process parameters that vary from case to case are given in Table 2. Case 1 and case 2 correspond to the grain-refined and non-grain-refined billets, respectively. The nucleation law used for the grain-refined billet (case 1) is evaluated based on the measured size distribution of an Al-Ti-B grain refiner [28], while that used for the non-grain-refined billet (case 2) is adjusted based on the experimental observation reported by Vreeman et al. [21]. Cases 3–6 are designed to study the effects of the casting speed and casting temperature on the non-grain-refined billet. For each case, fully coupled and transient simulation is performed, and the grain structure and macrosegregation in the entire billet are predicted.

Table 1. Simulation parameters for Al-6.0 wt % Cu alloy [21].

Parameter Description	Symbol	Unit	Value
Phase diagram (Al-Cu)			
Melting temperature of pure Al	T_f	K	933.5
Eutectic temperature	T_e	K	821.4
Eutectic composition	C_e	wt %	33.0
Partition coefficient	k_p	–	0.171
Thermophysical properties			
Density	ρ_m	$\mathrm{kg \cdot m^{-3}}$	2573.0
Specific heat of the liquid	c_{pl}	$\mathrm{J \cdot kg^{-1} \cdot K^{-1}}$	1045.0
Specific heat of the solid	c_{ps}	$\mathrm{J \cdot kg^{-1} \cdot K^{-1}}$	950.0
Thermal conductivity of the liquid	λ_l	$\mathrm{W \cdot m^{-1} \cdot K^{-1}}$	95.0
Thermal conductivity of the solid	λ_s	$\mathrm{W \cdot m^{-1} \cdot K^{-1}}$	162.0
Latent heat of fusion	$\Delta_s^l H_f$	$\mathrm{J \cdot kg^{-1}}$	3.87×10^5
Dynamic viscosity of the liquid	μ_l	Pa·s	0.0014
Diffusion coefficient in the liquid	D_l	$\mathrm{m^2 \cdot s^{-1}}$	5.0×10^{-9}
Thermal expansion coefficient of the liquid	β_T	$\mathrm{K^{-1}}$	1.17×10^{-4}
Solutal expansion coefficient of the liquid	β_C	$\mathrm{wt\,\%^{-1}}$	-9.0×10^{-3}
Process parameters			
Mold height	L_{mold}	m	0.07
Heat transfer coefficient, mold	h_{mold}	$\mathrm{W \cdot m^{-2} \cdot K^{-1}}$	30
Heat transfer coefficient, starter block	h_b	$\mathrm{W \cdot m^{-2} \cdot K^{-1}}$	400
Cooling water temperature	T_c	K	300
Additional parameters			
Gibbs-Thomson coefficient	Γ	m·K	1.96×10^{-7}
FE time step	Δt	s	0.05
FE element size	l_{FE}	m	2.5×10^{-3}
CA cell size	l_{CA}	m	2.5×10^{-4}

Table 2. Process parameters for different cases.

Case	v_{cast} (mm/s)	T_{cast} (K)	ΔT_N^V (K), ΔT_σ^V (K), n_{max}^V
1	1.0	943.35	$1.175, 0.5, 1.0 \times 10^{12}$
2	1.0	943.35	$5.0, 0.5, 1.0 \times 10^{10}$
3	0.8	943.35	$5.0, 0.5, 1.0 \times 10^{10}$
4	1.2	943.35	$5.0, 0.5, 1.0 \times 10^{10}$
5	1.0	920.0	$5.0, 0.5, 1.0 \times 10^{10}$
6	1.0	970.0	$5.0, 0.5, 1.0 \times 10^{10}$

4. Results and Discussion

4.1. Comparisons to Experimental Measurements

A validation is performed by comparisons to the experimental measurements reported by Vreeman et al. [21]. Figure 2 presents a comparison of the vertical temperature profiles at three different radiuses of 0.06 m, 0.12 m, and 0.22 m in the grain-refined billet. Due to the hot-top mold design, the radial heat extraction by mold (primary cooling) is very weak, resulting in a relatively slow decline near the inlet for all the three profiles. With the increasing distance to the inlet, the temperature at the subsurface (0.06 m), midradius (0.12 m), and centerline (0.22 m) decrease rapidly since 0.02 m, 0.12 m, and 0.22 m, respectively. This can be attributed to the strong heat extraction induced by the water jets (secondary cooling). Furthermore, it is notable that the two profiles at the midradius and centerline are very close when the distance to the inlet is less than 0.12 m, indicating a very uniform temperature distribution at the sump center.
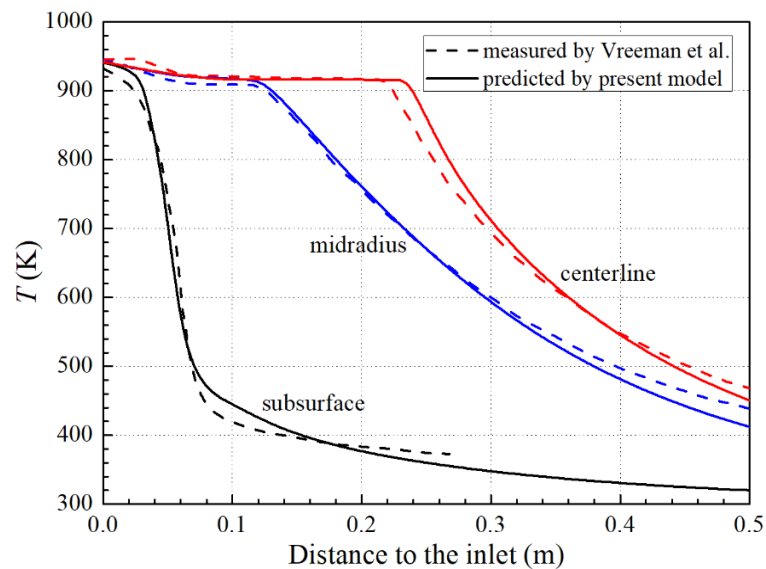
Figure 2. Comparison of the vertical temperature profiles predicted by present model and measured by Vreeman et al. [21] at three different radiuses in the grain-refined billet (case 1).

The steady sump profiles in the grain-refined billet are compared in Figure 3. The predicted sump profile is reasonably agreed with the measured one. The predicted profile is steeper near the surface and shallower near the center than the measured one. Moreover, the predicted sump depth is 0.216 m, while the measured value is 0.197 m. This may be attributed to an underestimated thermal conductivity or heat extraction in the secondary cooling region. Generally, the predicted vertical temperature and sump profiles are consistent with the experimental results to a certain extent. The discrepancy between the predicted and measured results can be mainly attributed to the simplified physical properties, and the use of an empirical thermal boundary condition proposed by Vreeman et al. [12].
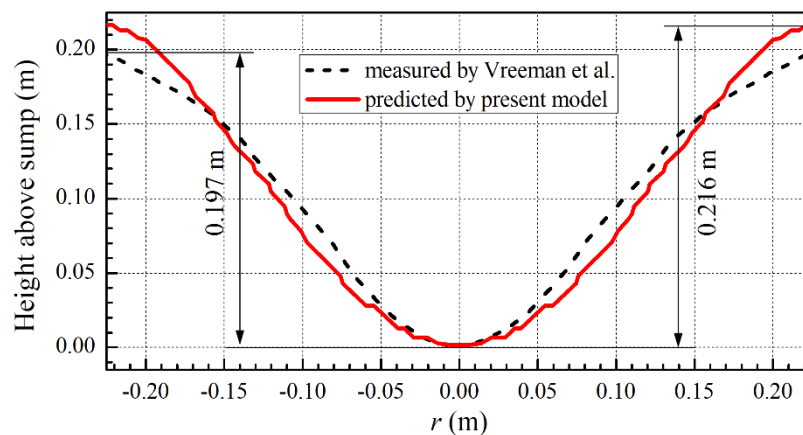

Figure 3. Comparison of the sump profiles ($f_s = 0$) predicted by present model and measured by Vreeman et al. [21] in the grain-refined billet (case 1).

4.2. Solidification Process of the Grain-Refined Billet

The transient DC casting process of the grain-refined billet (case 1) is analyzed in this section. Figure 4 shows the evolutions of the temperature field and the mushy zone in the first 830 s, when the billet grows to the maximum height of 900 mm. The mushy zone is confined by the blue isolines of $f_s = 0$ and $f_s = 1$. Due to the strong heat extraction in the secondary cooling region and relatively weak heat extraction at the bottom surface, the temperature decreases rapidly near the sidewall below the mold, while it drops slowly near the bottom surface (Figure 4a). The temperature gradient is very

large near the sidewall, from which a solid shell forms. In the billet center, however, the temperature is much more homogeneous. Moreover, it is notable that the isotherms in the mushy zone are unsmooth, which may be attributed to the undercooling and instability during grain growth [20]. With further cooling for the growing billet, the temperature gradient near the sidewall decreases, and the mushy zone moves towards the center, as shown in Figure 4b,c. A relatively steady sump profile characterized by a roughly triangular shape has been formed at 300 s (Figure 4c). It is obvious that the axial height of the mushy zone increases toward the center. At 830 s (Figure 4d), the isotherms are obviously not perpendicular to the bottom surface, which indicates a non-zero temperature gradient at the bottom surface, thus the DC casting process is not steady with regard to the temperature field.
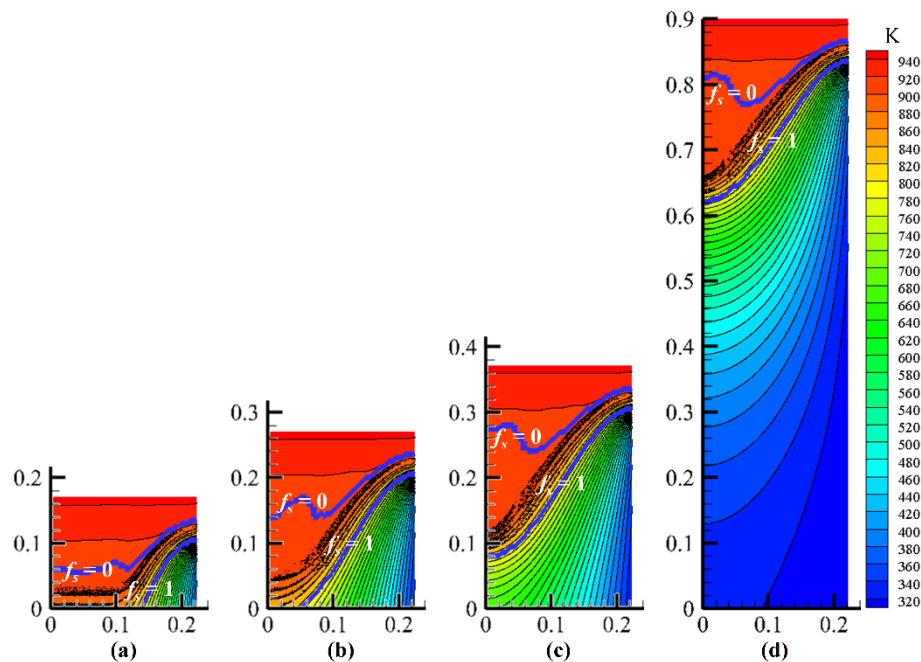

Figure 4. Evolutions of the temperature field and mushy zone predicted in the grain-refined billet (case 1): (**a**) 100 s, (**b**) 200 s, (**c**) 300 s, and (**d**) 830 s.

The evolution of the grain structure predicted in the grain-refined billet is shown in Figure 5. With the addition of the grain refiner, the nucleation on heterogeneous particles is remarkably promoted with a high nuclei density and a small nucleation undercooling. As a consequence, a large number of nucleation events can be found in the liquid ahead of the growth front, and a structure with fully equiaxed grains is obtained, as asserted in [21]. The grain size is not uniform in both the axial and radial directions, indicating that a transient modeling is necessary. Moreover, obviously large grains are shown in a region close to the centerline, as shown in Figure 5e. This grain distribution was also found in a 7075 alloy billet with 200 mm diameter [1]. It may be attributed to a small undercooling caused by relatively high temperature and relatively low Cu composition in the region. On the contrary, fine grains are formed near the surface and the centerline. The fine grain region near the surface may be explained by the strong heat extraction in the secondary cooling region. For the fine grain region near the centerline, the solute enrichment may be responsible. Because a high Cu composition near the centerline not only allows a great constitutional undercooling to be achieved, but also reduces the grain growth velocity, thus, more grains can be nucleated, resulting in fine grains.
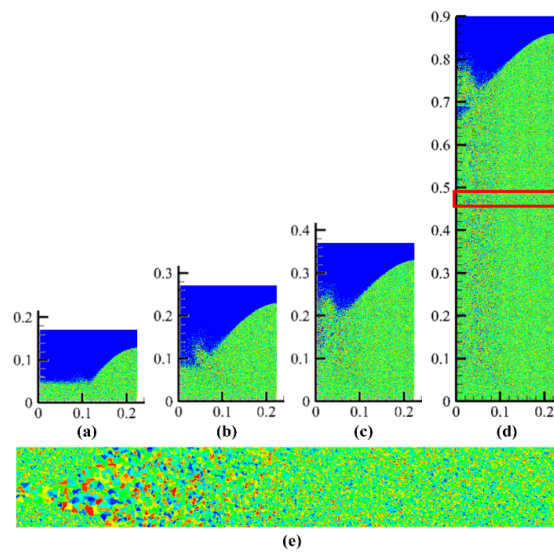
Figure 5. Evolution of the grain structure predicted in the grain-refined billet (case 1): (**a**) 100 s, (**b**) 200 s, (**c**) 300 s, (**d**) 830 s, with (**e**) the enlargement of grain structure confined by the red rectangle drawn in (**d**). Grains are distinguished by different colors.

The evolutions of the flow field and macrosegregation predicted in the grain-refined billet are shown in Figure 6. As the liquid of Al-6.0 wt % Cu alloy is characterized by a positive thermal expansion coefficient and a negative solute expansion coefficient, the thermal buoyancy and solutal buoyancy cooperate to drive a descending flow along the chilled surface (rigid solid) towards the centerline. The flow then turns upward at the center and runs towards the mold, resulting in a roughly triangular circulation in the sump. With the cooling of the growing billet, although the flow becomes more developed, the maximum velocity magnitude decreases gradually due to the decreasing temperature gradient near the chilled surface. Since the flow is induced only by thermal and solutal buoyancy in present model, the Cu composition shows an overall increase with the decrease of the radius. It is remarkable that the positive segregation near the centerline is less smooth, which may be attributed to the undercooling and instability during grain growth [20]. This calls into question the assumption that a steady state in the macrosegregation is truly reached during DC casting. Moreover, since the flow of the enriched liquid in the mushy zone is hold for a longer flow time due to the weak heat extraction, a negative segregation cone is formed near the bottom surface.
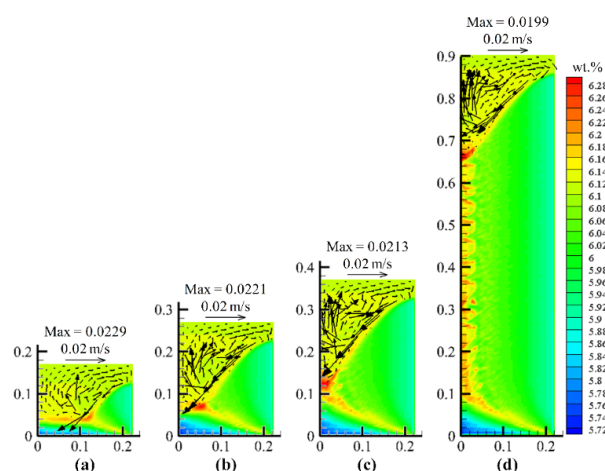

Figure 6. Evolutions of the flow field and macrosegregation predicted in the grain-refined billet (case 1): (**a**) 100 s, (**b**) 200 s, (**c**) 300 s, and (**d**) 830 s.

The radial Cu composition profile at the height of 500 mm predicted by present model is compared with the steady state one calculated by Vreeman et al. [21] in the non-grain-refined billet, in which the solid is assumed as rigid, as shown in Figure 7. Both profiles give an overall tendency that the average composition increases toward the centerline, showing a negative segregation near the surface and a positive segregation near the centerline. However, the predicted profile by present model shows a significantly lower composition near the centerline, and an obvious composition fluctuation is observed near the centerline, which is correlated to the unsmooth composition contour shown in Figure 6. As the main difference between the present model and the model given by Vreeman et al. [21], the coupling of grain structure and macrosegregation may be responsible for this discrepancy. Moreover, the predicted profile by present model is smooth near the surface, while that calculated by Vreeman et al. [21] shows a significant oscillation.
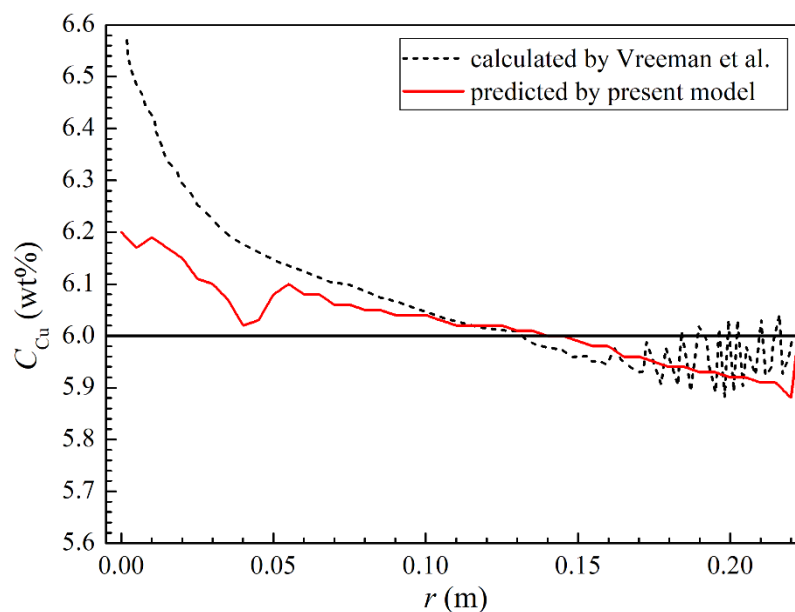
Figure 7. Radial Cu composition profiles predicted by present model at the height of 500 mm and calculated by Vreeman et al. [21] at steady state in the non-grain-refined billet (case 2).

4.3. Effects of the Casting Speed and Casting Temperature

The casting speed and casting temperature are two important process parameters in practice. This section is dedicated to clarify the effects of the casting speed and casting temperature on the grain structure and macrosegregation in the non-grain-refined billet, in which a CET was suspected. Case 2 corresponds to the non-grain-refined billet DC cast experimentally [27]. With identical configurations to case 2, only the casting speed or the casting temperature is modified in cases 3–6.

4.3.1. Effects of the Casting Speed

With the same casting temperature but three different casting speeds of 0.8 mm/s (case 3), 1.0 mm/s (case 2), and 1.2 mm/s (case 4), the billet reaches the maximum height of 900 mm at 1037.5 s, 830 s, and 691.7 s, respectively. The predicted grain structures are shown in Figure 8. They are all characterized by a fine equiaxed grain region near the surface, a fine equiaxed grain region near the centerline, and a fine columnar grain region between them, as shown in Figure 8a–c. Moreover, coarse columnar grains are formed near the bottom surface due to the small undercooling. The first fine equiaxed grain region can be attributed to the high undercooling caused by the strong heat extraction in the secondary cooling region. The second one is correlated to the constitutional undercooling caused by the enrichment of Cu composition in the liquid. With a relatively small undercooling and a relatively low composition in the middle part of the billet, the nucleation is suppressed and the grain growth

is promoted, leading to the fine columnar grain region. It is notable that the grain size decreases remarkably with the increasing casting speed, especially for the columnar grain region. Figure 8d presents the three profiles outlining the growth front and their normal vectors at the midradius, which are closely related to the growth directions. It is shown that the angle between the normal vector and the axis increases with the increasing casting speed, indicating that the columnar grains grow more perpendicular to the axis. In addition, the two fine equiaxed grain regions near the surface and the centerline imply that the assumption of a rigid solid is not valid even in the non-grain-refined billet.
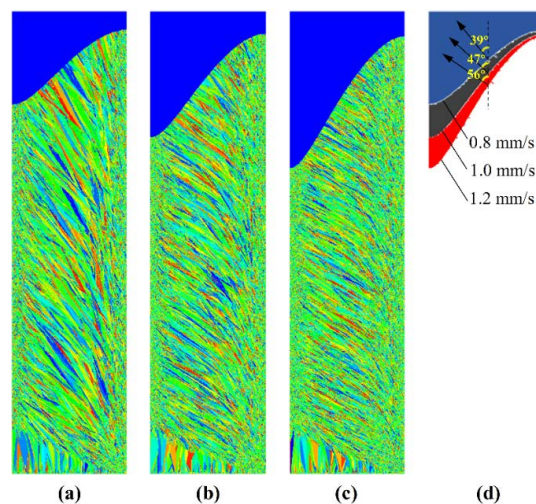

(a) (b) (c) (d)

Figure 8. Grain structures predicted in the non-grain-refined billet with different casting speeds of (**a**) 0.8 mm/s (case 3), (**b**) 1.0 mm/s (case 2), and (**c**) 1.2 mm/s (case 4), accompanied with (**d**) the growth front profiles when the maximum height is reached.

The final macrosegregation maps in the three cases are shown in Figure 9. It is obvious that the sump depth and steepness increase with the increasing casting speed, resulting in a more intense flow in the sump. As the macrosegregation is closely related to the liquid flow in the mushy zone and the sump depth, the positive segregation near the centerline is more pronounced with the increasing casting speed.
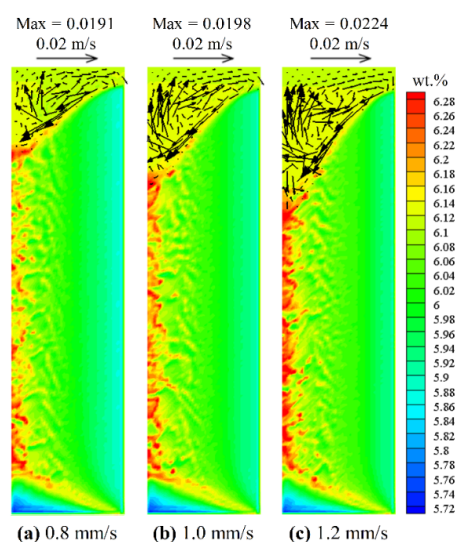

(**a**) 0.8 mm/s (**b**) 1.0 mm/s (**c**) 1.2 mm/s

Figure 9. Macrosegregation maps predicted in the non-grain-refined billet with different casting speeds of (**a**) 0.8 mm/s (case 3), (**b**) 1.0 mm/s (case 2), and (**c**) 1.2 mm/s (case 4) when the maximum height is reached.

4.3.2. Effects of the Casting Temperature

With the same casting speed, three different casting temperatures of 920 K (case 5), 943.35 K (case 2), and 970 K (case 6) are considered here. For each case, the billet reaches the maximum height of 900 mm at the same time of 830 s. The predicted grain structures are shown in Figure 10. They are also composed of a fine equiaxed grain region near the surface, a fine equiaxed grain region near the centerline, a fine columnar grain region in the middle part, and a coarse columnar grain region near the bottom surface (Figure 10a–c). As the increasing melt temperature reduces the undercooling, the grains tend to coarsen. The area of the fine equiaxed grain region decreases, and that of the columnar grain region increases. However, little difference is found in the growth direction of the columnar grains. Figure 10d presents the growth front profiles. Although the profile depth slightly increases with the increasing casting temperature, its shape remains almost unchanged, which explains the little difference in the growth direction of the columnar grains. Moreover, because the columnar grains grow in a direction close to the normal vector of the growth front, the growth direction is more parallel to the axis direction with the closer to the surface, as shown in Figure 10c.
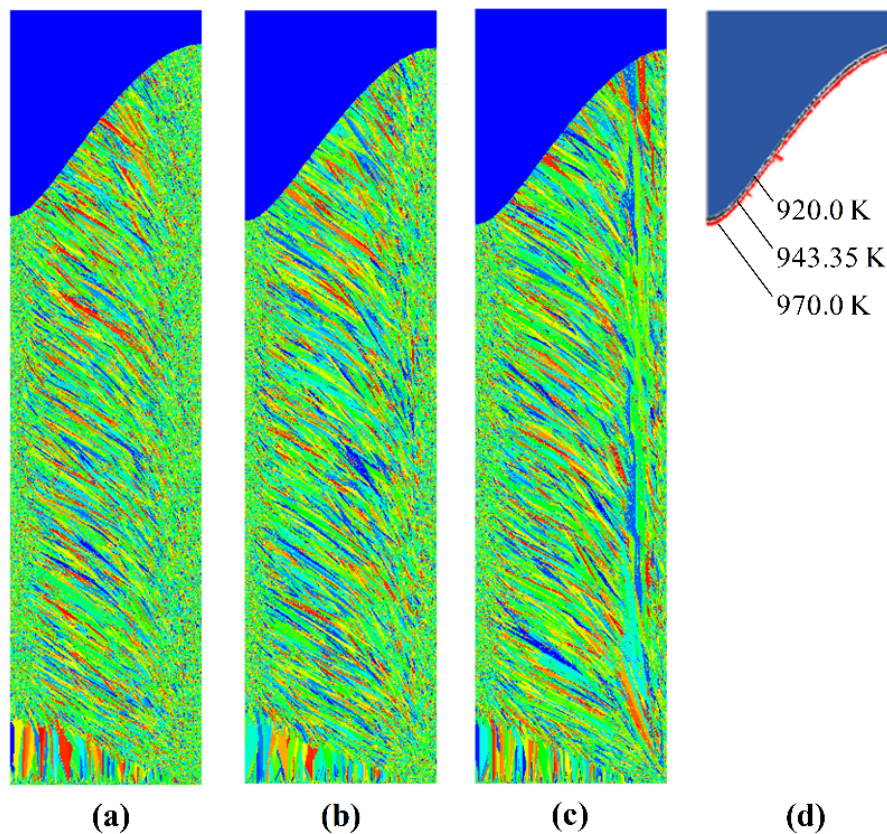

Figure 10. Grain structures predicted in the non-grain-refined billet with three different casting temperatures of (**a**) 920 K (case 5), (**b**) 943.35 K (case 2), and (**c**) 970 K (case 6), accompanied with (**d**) the growth front profiles when the maximum height is reached.

The final macrosegregation maps in the three cases are shown in Figure 11. As more heat needs to be removed and higher temperature differences are imposed, the flow intensity increases significantly with the increasing casting temperature. However, little change can be seen about the sump profile, thus, the positive segregation near the centerline remains virtually unaffected. In contrast, the negative segregation near the surface becomes more pronounced due to a wider mushy zone with a stronger flow in the mushy zone.
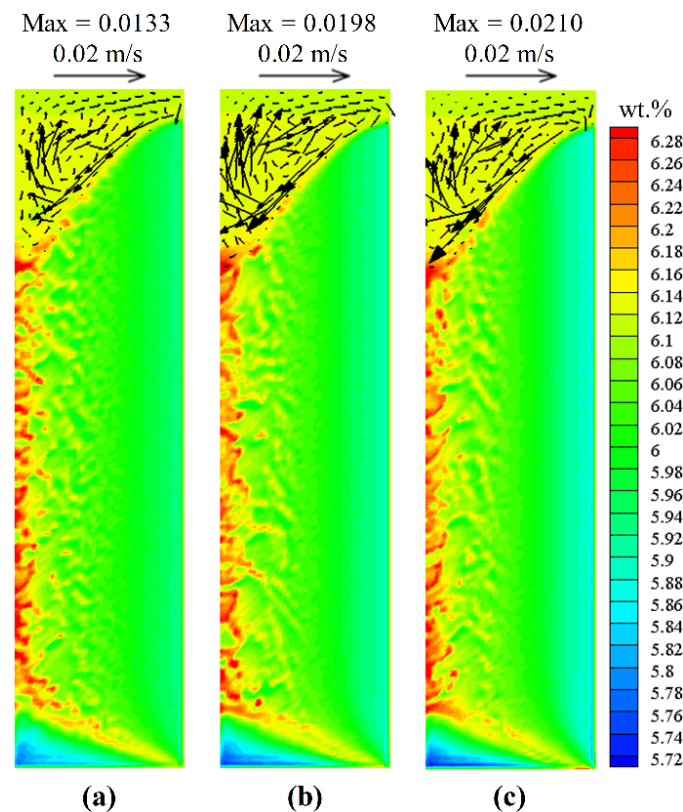
Figure 11. Macrosegregation maps predicted in the non-grain-refined billet with different casting temperatures of (**a**) 920 K (case 5), (**b**) 943.35 K (case 2), and (**c**) 970 K (case 6) when the maximum height is reached.

5. Conclusions

Transient modeling of the grain structure and macrosegregation during direct chill (DC) casting of two industrial scale Al-6.0 wt % Cu round billets with and without grain refiner has been achieved with a cellular automaton (CA)—finite element (FE) model. In this model, one-phase continuum mixture model is adopted for the macroscopic transport of mass, momentum, energy, and solute. It is solved by a FE method and coupled with a CA method, by which the nucleation, grain growth, and the dendrite tip growth kinetics are considered. With a two-dimensional (2D) axisymmetric description, a Lagrangian representation is used for both FE and CA calculations. Thus, the billet is treated to grow upward by extending the calculation domain from the top surface. Fully coupled and transient simulations are performed, and the grain structure and macrosegregation induced by thermal and solutal convection in the entire billet are investigated. The results are summarized as follows:

(1) With regard to the temperature field, flow field, grain structure and macrosegregation, a strictly steady state is not reached, indicating the importance of transient modeling.

(2) Fully equiaxed grains are obtained in the grain-refined billet, and the grains are coarser in a region close to the centerline. In contrast, a fine columnar grain region and a coarse columnar grain region are obtained in the middle part and bottom part of the non-grain-refined billet. The equiaxed grains found in the two billets imply a requirement for the numerical model to consider the motion of equiaxed grains.

(3) With the increasing casting speed, the sump depth and steepness increase remarkably, resulting in a more intense flow field and a more pronounced positive segregation near the centerline. Grains tend to be finer and grow in a direction more perpendicular to the symmetry axis. With the increasing casting temperature, the sump profile remains almost unaffected, and grains tend to be coarser.

The flow intensity increases significantly and the negative segregation near the centerline becomes more pronounced.

Author Contributions: Conceptualization: Q.C. and H.S.; data curation: Q.C.; formal analysis: Q.C.; funding acquisition: H.S.; investigation: Q.C., H.L., and H.S.; methodology: Q.C. and H.S.; project administration: H.S.; resources: H.S.; software: Q.C.; supervision: H.S.; validation, Q.C., H.L., and H.S.; visualization: Q.C., H.L., and H.S.; writing—original draft: Q.C.; writing—review and editing: Q.C., H.L., and H.S.

Conflicts of Interest: The authors declare no conflict of interest.

References

1. Nadella, R.; Eskin, D.G.; Du, Q.; Katgerman, L. Macrosegregation in direct-chill casting of aluminium alloys. *Prog. Mater. Sci.* **2008**, *53*, 421–480. [CrossRef]

2. Lesoult, G.; Albert, V.; Appolaire, B.; Combeau, H.; Daloz, D.; Joly, A.; Stomp, C.; Gruen, G.U.; Jarry, P. Equi-axed growth and related segregations in cast metallic alloys. *Sci. Technol. Adv. Mater.* **2001**, *2*, 285–291. [CrossRef]

3. Glenn, A.M.; Russo, S.P.; Paterson, P. The effect of grain refining on macrosegregation and dendrite arm spacing of direct chill cast AA5182. *Metall. Mater. Trans. A* **2003**, *34A*, 1513–1523. [CrossRef]

4. Suyitno; Eskin, D.G.; Savran, V.I.; Katgerman, L. Effects of alloy composition and casting speed on structure formation and hot tearing during direct-chill casting of Al-Cu alloys. *Metall. Mater. Trans. A* **2004**, *35A*, 3551–3561. [CrossRef]

5. Eskin, D.G.; Zuidema, J.; Savran, V.I.; Kategerman, L. Structure formation and macro segregation under different process conditions during DC casting. *Mat. Sci. Eng. A Struct.* **2004**, *384*, 232–244. [CrossRef]

6. Eskin, D.G.; Savran, V.I.; Katgerman, L. Effects of melt temperature and casting speed on the structure and defect formation during direct-chill casting of an Al-Cu alloy. *Metall. Mater. Trans. A* **2005**, *36A*, 1965–1976. [CrossRef]

7. Nadella, R.; Eskin, D.G.; Katgerman, L. Effect of grain refinement on structure evolution, "Floating" grains, and centerline macrosegregation in direct-chill cast AA2024 alloy billets. *Metall. Mater. Trans. A* **2008**, *39A*, 450–461. [CrossRef]

8. Eskin, D.G.; Nadella, R.; Katgerman, L. Effect of different grain structures on centerline macrosegregation during direct-chill casting. *Acta Mater.* **2008**, *56*, 1358–1365. [CrossRef]

9. Eskin, D.G.; Jafari, A.; Katgerman, L. Contribution of forced centreline convection during direct chill casting of round billets to macrosegregation and structure of binary Al-Cu aluminium alloy. *Mater. Sci. Technol.* **2011**, *27*, 890–896. [CrossRef]

10. Flood, S.C.; Katgerman, L.; Voller, V.R. The calculation of macrosegregation and heat and fluid flows in the DC casting of aluminum alloys. In *Modeling of Casting, Welding and Advanced Solidification Processes V*; Rappaz, M., Ozgu, M.R., Mahin, K.W., Eds.; TMS: Warrendale, PA, USA, 1991; pp. 683–690.

11. Vreeman, C.J.; Krane, M.J.M.; Incropera, F.P. The effect of free-floating dendrites and convection on macrosegregation in direct chill cast aluminum alloys: Part I: Model development. *Int. J. Heat Mass Transf.* **2000**, *43*, 677–686. [CrossRef]

12. Vreeman, C.J.; Incropera, F.P. The effect of free-floating dendrites and convection on macrosegregation in direct chill cast aluminum alloys: Part II: Predictions for Al–Cu and Al–Mg alloys. *Int. J. Heat Mass Transf.* **2000**, *43*, 687–704. [CrossRef]

13. Zaloznik, M.; Sarler, B. Modeling of macrosegregation in direct-chill casting of aluminum alloys: Estimating the influence of casting parameters. *Mat. Sci. Eng. A Struct.* **2005**, *413*, 85–91. [CrossRef]

14. Du, Q.; Eskin, D.G.; Katgerman, L. Modeling macrosegregation during direct-chill casting of multicomponent aluminum alloys. *Metall. Mater. Trans. A* **2007**, *38*, 180–189. [CrossRef]

15. Reddy, A.V.; Beckermann, C. Modeling of macrosegregation due to thermosolutal convection and contraction-driven flow in direct chill continuous casting of an Al-Cu round ingot. *Metall. Mater. Trans. B* **1997**, *28*, 479–489. [CrossRef]

16. Zaloznik, M.; Kumar, A.; Combeau, H.; Bedel, M.; Jarry, P.; Waz, E. The coupling of macrosegregation with grain nucleation, growth and motion in DC cast aluminium alloy ingots. In *Light Metals 2011*; TMS 2011, San Diego, California, United State; Lindsay, S.J., Ed.; Springer: Cham, Switzerland, 2011; pp. 699–704.

17. Heyvaert, L.; Bedel, M.; Zaloznik, M.; Combeau, H. Modeling of the coupling of microstructure and macrosegregation in a direct chill cast Al-Cu billet. *Metall. Mater. Transf. A* **2017**, *48*, 4713–4734. [CrossRef]

18. Williams, A.J.; Croft, T.N.; Cross, M. Modeling of ingot development during the start-up phase of direct chill casting. *Metall. Mater. Transf. B* **2003**, *34*, 727–734. [CrossRef]

19. Fezi, K.; Plotkowski, A.; Krane, M.J.M. Macrosegregation modeling during direct-chill casting of aluminum alloy 7050. *Numer. Heat Transf. A Appl.* **2016**, *70*, 939–963. [CrossRef]

20. Chen, Q.P.; Shen, H.F. Direct macroscopic modeling of grain structure and macrosegregation with a cellular automaton–finite element model. *Metals* **2019**, *9*, 177. [CrossRef]

21. Vreeman, C.J.; Schloz, J.D.; Krane, M.J.M. Direct chill casting of aluminum alloys: Modeling and experiments on industrial scale ingots. *J. Heat Transf.* **2002**, *124*, 947–953. [CrossRef]

22. Bennon, W.D.; Incropera, F.P. A continuum model for momentum, heat and species transport in binary solid liquid-phase change systems. 1. Model formulation. *Int. J. Heat Mass Transf.* **1987**, *30*, 2161–2170. [CrossRef]

23. Thevoz, P.; Desbiolles, J.L.; Rappaz, M. Modeling of equiaxed microstructure formation in casting. *Metall. Trans. A* **1989**, *20*, 311–322. [CrossRef]

24. Rappaz, M.; Gandin, C.A. Probabilistic modeling of microstructure formation in solidification processes. *Acta Mater.* **1993**, *41*, 345–360. [CrossRef]

25. Guillemot, G.; Gandin, C.A.; Combeau, H. Modeling of macrosegregation and solidification grain structures with a coupled cellular automaton-finite element model. *ISIJ Int.* **2006**, *46*, 880–895. [CrossRef]

26. Gandin, C.A.; Guillemot, G.; Appolaire, B.; Niane, N.T. Boundary layer correlation for dendrite tip growth with fluid flow. *Mater. Sci. Eng. A Struct.* **2003**, *342*, 44–50. [CrossRef]

27. Chen, Q.P.; Shen, H.F. A finite element formulation for macrosegregation during alloy solidification using a fractional step method and equal-order elements. *Comput. Mater. Sci.* **2018**, *154*, 335–345. [CrossRef]

28. Bedel, M.; Tveito, K.O.; Zaloznik, M.; Combeau, H.; M'Hamdi, M. A model study of the impact of the transport of inoculant particles on microstructure formation during solidification. *Comp. Mater. Sci.* **2015**, *102*, 95–109. [CrossRef]